

Article

# Exploration of Darcy–Forchheimer Flows of Non-Newtonian Casson and Williamson Conveying Tiny Particles Experiencing Binary Chemical Reaction and Thermal Radiation: Comparative Analysis

Sheniyappan Eswaramoorthi <sup>1</sup>, S. Thamaraiselvi <sup>1</sup> and Karuppusamy Loganathan <sup>2,3,\*</sup> 

<sup>1</sup> Department of Mathematics, Dr. N.G.P. Arts and Science College, Coimbatore 641035, India; eswaramoorthi@drngpasc.ac.in (S.E.); 202ma022@drngpasc.ac.in (S.T.)

<sup>2</sup> Department of Mathematics and Statistics, Manipal University Jaipur, Jaipur 303007, India

<sup>3</sup> Research and Development Wing, Live4Research, Tiruppur 638106, India

\* Correspondence: loganathankaruppusamy304@gmail.com

**Abstract:** This discussion intends to scrutinize the Darcy–Forchheimer flow of Casson–Williamson nanofluid in a stretching surface with non-linear thermal radiation, suction and heat consumption. In addition, this investigation assimilates the influence of the Brownian motion, thermophoresis, activation energy and binary chemical reaction effects. Cattaneo–Christov heat-mass flux theory is used to frame the energy and nanoparticle concentration equations. The suitable transformation is used to remodel the governing PDE model into an ODE model. The remodeled flow problems are numerically solved via the BVP4C scheme. The effects of various material characteristics on nanofluid velocity, nanofluid temperature and nanofluid concentration, as well as connected engineering aspects such as drag force, heat, and mass transfer gradients, are also calculated and displayed through tables, charts and figures. It is noticed that the nanofluid velocity upsurges when improving the quantity of Richardson number, and it downfalls for larger magnitudes of magnetic field and porosity parameters. The nanofluid temperature grows when enhancing the radiation parameter and Eckert number. The nanoparticle concentration upgrades for larger values of activation energy parameter while it slumps against the reaction rate parameter. The surface shear stress for the Williamson nanofluid is greater than the Casson nanofluid. There are more heat transfer gradient losses the greater the heat generation/absorption parameter and Eckert number. In addition, the local Sherwood number grows when strengthening the Forchheimer number and fitted rate parameter.

**Keywords:** Casson and Williamson fluid; MHD; Cattaneo–Christov dual flux; non-linear thermal radiation; binary chemical reaction



**Citation:** Eswaramoorthi, S.; Thamaraiselvi, S.; Loganathan, K. Exploration of Darcy–Forchheimer Flows of Non-Newtonian Casson and Williamson Conveying Tiny Particles Experiencing Binary Chemical Reaction and Thermal Radiation: Comparative Analysis. *Math. Comput. Appl.* **2022**, *27*, 52. <https://doi.org/10.3390/mca27030052>

Academic Editors: Mehmet Yavuz and Ioannis Dassios

Received: 23 May 2022

Accepted: 17 June 2022

Published: 20 June 2022

**Publisher’s Note:** MDPI stays neutral with regard to jurisdictional claims in published maps and institutional affiliations.



**Copyright:** © 2022 by the authors. Licensee MDPI, Basel, Switzerland. This article is an open access article distributed under the terms and conditions of the Creative Commons Attribution (CC BY) license (<https://creativecommons.org/licenses/by/4.0/>).

## 1. Introduction

Nowadays, heat transfer enrichment is a fascinating topic because of its numerous applications in engineering and industry. In many industrial processes, regular fluids (water, oil and ethylene glycol) are often employed. However, these fluids have a low heat transfer phenomenon because of their low thermal conductivity. To address this shortcoming, the nanometer-sized particle was mixed with regular fluids and enriches the regular fluid thermal conductivity; see [1–3]. This is the way of preparing the nanofluid, and this fluid has played an essential role in many fields such as solar water heating, heat exchangers, transformer cooling, cancer therapy, etc. Choi [4] was the first to publish the characteristics of nanoparticles, which were coupled with experimental evidence data. The nanofluid flow over a cylinder with suction was explored by Sheikholeslami [5]. It was uncovered that the local Nusselt number elevates when mounting the nanoparticle volume fraction values. Ramana Reddy et al. [6] addressed the time-dependent MHD flow of

nanofluid past a slendering surface. It was detected that the fluid temperature progressed when enhancing the Brownian motion parameter. Makinde et al. [7] employed the impact of Brownian motion and thermophoresis effects of MHD flow of nanofluid past a heated surface. It was noted that the heat transfer rate decays when upturning the quantity of the Brownian motion parameter. The consequences of Brownian motion and thermophoresis of stagnation point flow of nanofluid past a non-uniform cylinder were presented by Shafey et al. [8]. It was noticed that the heat transfer gradient slumps when rising the thermophoresis quantity. Rasheed et al. [9] addressed the MHD flow of water-based nanofluids with convective heating conditions. It was seen that the thermophoretic parameter improves the thickness of the thermal boundary layer.

The non-Newtonian fluid has stimulated various scientists to investigate the events of heat-mass transport because of its necessary part in industrial and engineering processes, such as drilling muds, polymer extrusion, optical fibers, polymer production, etc. The non-Newtonian fluid defies the Newton's viscosity law. To deal with the huge nature of the rheological behavior of such fluids, several non-Newtonian models have been devised. Casson fluid is one of the non-Newtonian type models, and at the infinite non-linear shear rate, the fluid material's yield stress does not push flow, and it has zero viscosity. The MHD flow of Casson nanofluid past a heated surface with viscous dissipation was analyzed by Alotaibi et al. [10]. It was found that the drag force coefficient decays when strengthening the Casson parameter. Nayak et al. [11] provide the impact of the triple diffusive bioconvective flow of Casson nanofluid past a sheet. It was observed that the wall motile micro-organism decimates when developing the Casson parameter. Entropy optimization of MHD flow of Casson nanofluid over a stretching surface with convective heating and mass conditions was illustrated by Butt et al. [12]. It was proved that the Casson fluid parameter leads to a slow down of the entropy production. Ibrahim et al. [13] discovered the chemically reactive MHD flow of Casson nanofluid past a stretching surface with viscous dissipation. It was noticed that the nanoparticle concentration profile decreases when raising the Casson parameter. The multiple slip effects of a Casson nanofluid on a stretching surface were numerically performed by Afify [14], and he proved that the mass transfer gradient enriches when enhancing the Casson parameter. Varun Kumar et al. [15] scrutinized the MHD chemically reactive flow of Casson nanofluid past a curved stretching sheet. It was noted that liquid velocity depresses when enhancing the Casson parameter. The 2D flow of Casson nanofluid on a thin moving needle was examined by Naveen Kumar et al. [16], and they proved that the thermophoresis parameter improves the mass transfer rate. Gohar et al. [17] studied the Darcy–Forchheimer flow of Casson hybrid nanofluid on a curved surface. It was detected that the Casson parameter suppresses the hybrid nanofluid motion.

Williamson fluid is also the non-Newtonian division model, which exhibits the shear thinning property; that is, the fluid viscosity decays when rising the shear stress rate. Waqas et al. [18] examined the MHD flow of Williamson nanofluid past a heated wedge. It was revealed that the wall shear stress downfalls when mounting the Weissenberg number. The MHD flow of Williamson nanofluid past a porous stretching surface with suction was presented by Li et al. [19]. It was noted that the Williamson parameter leads to deprecating the friction drag. Ahmed et al. [20] presented the consequences of MHD Williamson nanofluid flow on an exponentially porous stretching surface. It was uncovered that the fluid speed depresses when escalating the Williamson parameter. The 2D flow of Williamson fluid over a cylinder was addressed by Iqbal et al. [21], and it was acknowledged that the skin friction coefficient decreases as the Weissenberg number increases. Gorla and Gireesha [22] demonstrated the convective heat transport analysis of a Williamson nanofluid past the stretching surface. It was noticed that the nanofluid volume fraction intensifies when heightening the Williamson parameter. The MHD flow of Williamson nanofluid past a heated stretching surface was examined by Srinivasulu and Goud [23]. It was concluded that the heat transfer gradient downfalls when promoting the quantity of the Williamson parameter.

In the last few decades, many researchers have focused on studying the thermal radiation effect because the consequences of thermal radiation in flow structures are helpful in atomic reactors, spacecraft, ship compressors, and solar radiation. Most of the investigation is based on linearized Rosseland approximation; however, this concept is applicative when the temperature distinction between ambient and fluid is small. However, on many industrial occasions, this difference is enormous. So, a non-linearized Rosseland approximation is introduced to overcome this restriction. MHD Casson nanofluid in a bi-directional heated stretching surface with non-linear radiation was deliberated by Mahanta et al. [24]. It was detected that the temperature ratio parameter leads to enriching the entropy generation profile. Humane et al. [25] scrutinized the thermally radiative MHD Casson–Williamson nanofluid flow on a porous stretching surface with a chemical reaction. MHD heat-generating Casson nanofluid through a thin needle with non-linear thermal radiation was examined by Akinshilo et al. [26]. Ghasemi et al. [27] numerically solved the non-linear thermal radiative flow of nanofluid with a magnetic field via the spectral relaxation method. It was noted that the nanofluid concentration upsurges when enhancing the thermal radiation parameter. The bio-convective flow of Carreau nanofluid with non-linear thermal radiation with a magnetic dipole was presented by Imran et al. [28]. It was shown that the thermal boundary layer thickens when the temperature ratio parameter is large. Bhatti et al. [29] demonstrated the impact of MHD flow of Williamson nanofluid through a shrinking porous sheet. The problem of non-linear radiative flow of nanofluid with the inclined magnetic field was numerically solved via the finite difference method by Mahanthesh and Thriveni [30]. Their results clearly explain that the fluid temperature ascends when upgrading the quantity of the thermal radiation parameter. Cao et al. [31] investigated the non-linear thermal radiative flow of a ternary-hybrid nanofluid with partial slip. The 3D radiative flow of  $Cu/Ag$ -water-based nanofluid with entropy optimization was illustrated by Eswaramoorthi et al. [32], and they detected that the Bejan number rises as the radiation parameter enhances.

The smallest amount of energy necessary to start a chemical reaction is known as activation energy. This conception was initiated by Arrhenius in 1889, and this incident has plentiful appliances in geothermal engineering, water emulsions, oil emulsion and food processing. Shah et al. [33] addressed the chemically reactive flow of Casson nanofluid with activation energy and radiation, and they found that activation energy leads to magnifying the nanoparticle concentration. The 3D time-dependent flow of Williamson nanofluid with heat generation and the activation energy was inspected by Aziz et al. [34]. Their findings show that the higher chemical reaction parameter suppresses the nanofluid concentration. Kalaivanan et al. [35] discussed the Arrhenius activation energy and non-linear thermal impacts of second-grade nanofluid past a stretching surface. It was exposed that the heat transfer gradient weakens when strengthening the exponential fitted rate. The MHD flow of Casson nanofluid over a stretching cylinder with Arrhenius activation energy was examined by Zeeshan et al. [36]. It was seen that the nanoparticle concentration enhances for strengthening the activation energy parameter. Tayyab et al. [37] securitized the consequences of Darcy–Forchheimer flow of 3D nanofluid on a sheet with activation energy. The 3D Darcy–Forchheimer flow past a porous space with the presence of Arrhenius activation energy was presented by Rashid et al. [38]. It was revealed that the reaction rate leads to a decline in the nanoparticle concentration profile. Alsaadi et al. [39] elucidated the flow of MHD WNF with the influence of Arrhenius activation energy. The impact of activation energy of a second-grade nanofluid on a surface with heat source/sink was analyzed by Punith Gowda et al. [40]. Varun Kumar et al. [41] studied the impact of Arrhenius activation energy on a hybrid nanofluid past a curved surface. It was proved that the nanofluid concentration improves when escalating the activation energy parameter. The MHD flow of Williamson nanofluid with activation energy was investigated by Tamilzharasan et al. [42], and they found that the activation energy parameter improves the heat transfer rate.

In light of the above analysis, no research articles provide the impact of the non-linear thermal radiative flow of Casson–Williamson nanofluid over a heated stretchy plate with activation energy. In addition, zero nanoparticle mass flux and Cattaneo–Christov heat-mass flux conditions are included in our study. This research has implications for thermal sciences, food processing, chemical engineering, polymer extrusion, and many other fields in which heat conduction and convection are improved. In the limiting scenarios, the calculated values derived from specified parameters are consistent with existing findings in the literature, while tables and graphs have been built and explained to spread the responses of dimensionless quantities. This type of flow model is used in food processing, heavy mechanical apparatus, enzymes, ceramic processing, heating/cooling processes, etc.

### 2. Mathematical Formulation

Let us consider the chemically reactive 2D Darcy–Forchheimer flow of Casson–Williamson nanofluid past a stretchy plate. The  $x$ -axis is in the stretching direction and the  $y$ -axis is perpendicular to it. The uniform magnetic field of strength  $B_0$  is applied in the  $y$ -direction, and the induced magnetic effect is neglected because of the small quantity of Reynolds number. Moreover, the flow is disclosed under the consequences of Arrhenius activation energy; suction/injection, viscous dissipation and non-linear thermal radiation are all taken into our account. The zero nanoparticle mass flux condition is assumed on the surface of the sheet. Let  $T_w$  and  $C_w$  represent the temperature and nanoparticle concentration, which are higher than the free-stream temperature ( $T_\infty$ ) and nanoparticle concentration ( $C_\infty$ ), see Figure 1.

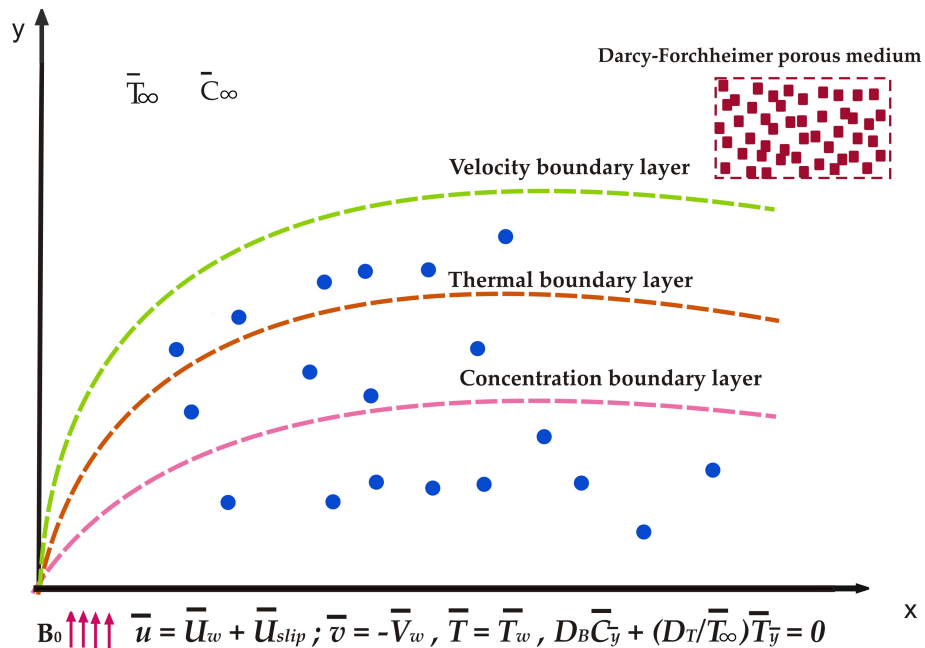


Figure 1. Physical model of flow.

The Cauchy stress tensor of Williamson fluid is expressed as  $S = -pI + \tau_1$ , where  $\tau_1 = \left[ \mu_\infty + \frac{(\mu_0 - \mu_\infty)}{1 - \Gamma_1 \gamma_1^*} \right] A_1$ ; here,  $\tau_1$  is the extra stress tensor,  $\mu_0$  is the limiting viscosity at zero shear rate,  $\mu_\infty$  is the limiting viscosity at infinity shear rate,  $\Gamma_1 > 0$  is the time constant and  $A_1$  is the Rivlin–Ericson tensor. The simplified form of the extra stress tensor is  $\tau_1 = \left[ + \frac{\mu_0}{1 - \Gamma_1 \gamma_1^*} \right] A_1$ ; see [43].

Similarly, Casson fluid flow is

$$\tau_{ij} = \begin{cases} 2\left(\mu_{nf} + \frac{Q_y}{\sqrt{2\pi}}\right)k_{ij}, & \pi > \pi_c \\ 2\left(\mu_{nf} + \frac{Q_y}{\sqrt{2\pi_c}}\right)k_{ij}, & \pi < \pi_c \end{cases}$$

here,  $Q_y$  is the yield stress of fluid,  $k_{ij}$  is the  $(i, j)$ th laceration direction component rate,  $\pi = k_{ij}k_{ij}$  is the product of the component of rate of deformation with itself and  $\pi_c$  is the critical value of the product of the component of the strain tensor rate with itself; see [44].

The flow model may be described as follows using the given assumptions; see Mustafa et al. [45].

$$\bar{u}_{\bar{x}} + \bar{v}_{\bar{y}} = 0 \tag{1}$$

$$\begin{aligned} \bar{u}\bar{u}_{\bar{x}} + \bar{v}\bar{u}_{\bar{y}} &= \nu \left(1 + \frac{1}{\beta}\right) \bar{u}_{\bar{y}\bar{y}} + \sqrt{2}\Gamma\nu\bar{u}_{\bar{y}}\bar{u}_{\bar{y}\bar{y}} - \frac{\nu}{k_1}\bar{u} - \frac{C_b}{\bar{x}\sqrt{k_1}}\bar{u}^2 - \frac{\sigma B_0^2\bar{u}}{\rho_f} \\ &+ \frac{1}{\rho_f} \left[ (1 - \bar{C}_\infty)\rho_{f\infty}\beta(\bar{T} - \bar{T}_\infty) - (\rho_p - \rho_{f\infty})(\bar{C} - \bar{C}_\infty) \right] g, \end{aligned} \tag{2}$$

$$\begin{aligned} \bar{u}\bar{T}_{\bar{x}} + \bar{v}\bar{T}_{\bar{y}} + \lambda_T\Omega_T &= \alpha\bar{T}_{\bar{y}\bar{y}} \\ &+ \frac{1}{\rho C_p} \frac{16\sigma^*}{3k^*} \frac{\partial}{\partial \bar{y}} \left(\bar{T}^3\bar{T}_{\bar{y}}\right) + \frac{Q}{\rho_f C_p} (\bar{T} - \bar{T}_\infty) + \tau \left[ D_B\bar{T}_{\bar{y}}\bar{C}_{\bar{y}} + \frac{D_T}{\bar{T}_\infty}\bar{T}_{\bar{y}}^2 \right] + \frac{\mu}{\rho C_p} \left(1 + \frac{1}{\beta}\right) \bar{u}_{\bar{y}}^2 \end{aligned} \tag{3}$$

$$\bar{u}\bar{C}_{\bar{x}} + \bar{v}\bar{C}_{\bar{y}} + \lambda_C\Omega_C = D_B\bar{C}_{\bar{y}\bar{y}} + \frac{D_T}{\bar{T}_\infty}\bar{C}_{\bar{y}\bar{y}} - k_r^2(\bar{C} - \bar{C}_\infty) \left(\frac{\bar{T}}{\bar{T}_\infty}\right)^n \exp\left(\frac{-E_a}{\kappa\bar{T}}\right) \tag{4}$$

where

$$\begin{aligned} \Omega_T &= \bar{u}\bar{u}_{\bar{x}}\bar{T}_{\bar{x}} + \bar{v}\bar{v}_{\bar{y}}\bar{T}_{\bar{y}} + \bar{u}^2\bar{T}_{\bar{x}\bar{x}} + \bar{v}^2\bar{T}_{\bar{y}\bar{y}} + 2\bar{u}\bar{v}\bar{T}_{\bar{x}\bar{y}} + \bar{u}\bar{v}_{\bar{x}}\bar{T}_{\bar{y}} + \bar{v}\bar{u}_{\bar{y}}\bar{T}_{\bar{x}} \\ \Omega_C &= \bar{u}\bar{u}_{\bar{x}}\bar{C}_{\bar{x}} + \bar{v}\bar{v}_{\bar{y}}\bar{C}_{\bar{y}} + \bar{u}^2\bar{C}_{\bar{x}\bar{x}} + \bar{v}^2\bar{C}_{\bar{y}\bar{y}} + 2\bar{u}\bar{v}\bar{C}_{\bar{x}\bar{y}} + \bar{u}\bar{v}_{\bar{x}}\bar{C}_{\bar{y}} + \bar{v}\bar{u}_{\bar{y}}\bar{C}_{\bar{x}} \end{aligned}$$

The boundary conditions are

$$\begin{aligned} \bar{u} &= \bar{U}_\omega + L \left(1 + \frac{1}{\beta} + \Gamma\bar{u}_{\bar{y}}\right) \bar{u}_{\bar{y}}; \bar{v} = -\bar{V}_\omega\bar{T} = \bar{T}_\omega, D_B\bar{C}_{\bar{y}} + \frac{D_T}{\bar{T}_\infty}\bar{T}_{\bar{y}} = 0 \text{ as } \bar{y} = 0 \\ \bar{u} &\rightarrow 0, \bar{T} \rightarrow \bar{T}_\infty, \bar{C} \rightarrow \bar{C}_\infty \text{ as } \bar{y} \rightarrow \infty \end{aligned} \tag{5}$$

From the above Equations (Equations (2) and (5)),  $\beta \rightarrow \infty$  &  $\Gamma \neq 0$  is treated as a Williamson fluid model and  $\beta \neq \infty$  &  $\Gamma = 0$  is treated as a Casson fluid model.

The dimensionless parameters are

$$\begin{aligned} \omega &= \sqrt{\frac{a}{\nu}}\bar{y}; \bar{u} = a\bar{x}v'_1; \bar{v} = -\sqrt{a\nu}v_1(\omega) \\ v_2(\omega) &= \frac{\bar{T} - \bar{T}_\infty}{\bar{T}_\omega - \bar{T}_\infty}; v_3(\omega) = \frac{\bar{C} - \bar{C}_\infty}{\bar{C}_\infty} \end{aligned} \tag{6}$$

Substituting Equation (6) into Equations (2)–(4), we obtain

$$\left(1 + \frac{1}{\beta}\right)v_1'''(\omega) - v_1'^2(\omega) + v_1(\omega)v_1''(\omega) + Wev_1''(\omega)v_1'''(\omega) - \lambda v_1'(\omega) - Frv_1'^2(\omega) - Mv_1'(\omega) + Ri(v_2(\omega) - Nrv_3(\omega)) = 0 \tag{7}$$

$$\frac{1}{Pr}v_2''(\omega) + \frac{1}{Pr}\frac{4}{3}R[(\theta_w - 1)^3\{v_2''(\omega)v_2^3(\omega) + 3v_2^2(\omega)v_2'^2(\omega)\} + 3(\theta_w - 1)^2\{v_2''(\omega)v_2^2(\omega) + 2v_2(\omega)v_2'(\omega)^2\} + 3(\theta_w - 1)\{v_2''(\omega)v_2(\omega) + v_2'^2(\omega)\} + v_2''(\omega)] + v_1(\omega)v_2'(\omega) - \Gamma_T\{v_1(\omega)v_1'(\omega)v_2'(\omega) + v_1^2(\omega)v_2''(\omega)\} + Hgv_2 + \left(1 + \frac{1}{\beta}\right)Ecv_1'^2 + Nbv_2'v_3' + Ntv_2'^2 = 0 \tag{8}$$

$$\frac{1}{Sc}v_3''(\omega) + v_1(\omega)v_3'(\omega) - \Gamma_C\{v_1(\omega)v_1'(\omega)v_3'(\omega) + v_1^2(\omega)v_3''(\omega)\} + \frac{1}{Sc}\left(\frac{Nt}{Nb}\right)v_2''(\omega) - \sigma^{**}(1 + \delta v_2(\omega))^n v_3(\omega) \exp\left(\frac{-E}{1 + \delta v_2(\omega)}\right) = 0 \tag{9}$$

The covered boundary conditions are

$$v_1(0) = fw, v_1'(0) = 1 + K\left[1 + \frac{1}{\beta} + \frac{We}{\sqrt{2}}v_1''(0)\right]v_1'(0), v_2(0) = 1, Nbv_3'(0) + Ntv_2'(0) = 0$$

$$v_1'(\infty) \rightarrow 0, v_2(\infty) \rightarrow 0, v_3(\infty) \rightarrow 0 \tag{10}$$

The non-dimensional form of skin friction coefficient, local Nusselt number and local Sherwood number are expressed as

$$\frac{1}{2}Cf\sqrt{Re} = -\left[\left(1 + \frac{1}{\beta}\right)v_1''(0) + \frac{We}{2}v_1''^2(0)\right]; \frac{Nu}{\sqrt{Re}} = -\left[1 + \frac{4}{3}R\{1 + (\theta_w - 1)v_2(0)\}^3\right]v_2'(0)$$

$$\frac{Sh}{\sqrt{Re}} = \frac{Nb}{Nt}v_2'(0)$$

### 3. Numerical Solution

The derived ODE models (7)–(9) along with the conditions (10) are numerically solved by applying the MATLAB bvp4c scheme. Initially, the higher-order terms are converted into first-order terms, see [46,47].

Let  $v_1 = y_1, v_1' = y_2, v_1'' = y_3, v_1''' = y_3', v_2 = y_4, v_2' = y_5, v_2'' = y_5', v_3 = y_6, v_3' = y_7, v_3'' = y_7'$ .

$$y_1' = y_2$$

$$y_2' = y_3$$

$$y_3' = \frac{y_2^2 - y_1y_3 + \lambda y_2 + Fry_2^2 + My_2 - Ri[y_4 - Nry_6]}{\left(1 + \frac{1}{\beta}\right) + We y_3}$$

$$y_4' = y_5$$

$$A = -y_1y_5 + \Gamma_T y_1y_2y_5 - \frac{1}{Pr}\frac{4}{3}R[(3\theta_n - 1)^3y_4^2y_5^2 + 6(\theta_n - 1)^2y_4y_5^2 + 3(\theta_n - 1)y_5^2]$$

$$\begin{aligned}
 B &= -Hgy_4 - Nby_5y_7 - Nty_5^2 - \left(1 + \frac{1}{\beta}\right) Ecy_3^2 \\
 y_5' &= \frac{A + B}{\frac{1}{Pr} [1 + \frac{4}{3}R[1 + (\theta_n - 1)^3y_4^3 + 3(\theta_n - 1)^2y_4^2 + 3(\theta_n - 1)y_4]] - \Gamma_T y_1^2} \\
 y_6' &= y_7 \\
 C &= -y_1y_5 + \Gamma_T y_1y_2y_5 - \frac{1}{Pr} \frac{4}{3}R[(3\theta_n - 1)^3y_4^2y_5^2 + 6(\theta_n - 1)^2y_4y_5^2 + 3(\theta_n - 1)y_5^2] \\
 D &= -Hgy_4 - Nby_5y_7 - Nty_5^2 - \left(1 + \frac{1}{\beta}\right) Ecy_3^2 \\
 E &= \frac{1}{Pr} [1 + \frac{4}{3}R[1 + (\theta_n - 1)^3y_4^3 + 3(\theta_n - 1)^2y_4^2 + 3(\theta_n - 1)y_4]] - \Gamma_T y_1^2 \\
 y_7' &= \frac{-y_1y_7 + \Gamma_C y_1y_2y_7 - \left(\frac{1}{Sc}\right) \left(\frac{Nt}{Nb}\right) \left(\frac{C+D}{E}\right) + \sigma^{**} (1 + \delta y_4)^n y_6 \exp\left(\frac{-E}{1+\delta y_4}\right)}{\frac{1}{Sc} - \Gamma_C y_1^2}
 \end{aligned}$$

With the conditions

$$\begin{aligned}
 y_1(0) &= fw, \quad y_2(0) = 1 + K \left[1 + \frac{1}{\beta} + \frac{We}{\sqrt{2}} y_3(0)\right] y_3(0), \quad y_2(\infty) = 0, \\
 y_4(0) &= 1, \quad Nby_7(0) + Nty_5(0) = 0, \quad y_4(\infty) = 0, \quad y_6(\infty) = 0
 \end{aligned} \tag{11}$$

We implemented the MATLAB bvp4c scheme to find the numerical solution for the above problem with maximum error is  $10^5$  and step size is 0.05.

#### 4. Results and Discussion

This segment provides the details about the changes of velocity, temperature, naofluid concentration, skin friction coefficient (SFC), local Nusselt number (LNN) and local Sherwood number (LSN) for different flow parameters through graphs and tables. The consequences of  $fw, \lambda, Fr, M, Ri$  and  $Nr$  (Table 1),  $R, Hg, Ec, \Gamma_T, Nb, Nt$  and  $\theta_n$  (Table 2) and  $\Gamma_c, \sigma^{**}, \delta, n$  and  $E$  (Table 3) on SFC, LNN and LSN for Casson–Williamson nanofluid are deliberated in Tables 1–3. Table 4 provides the comparison of our numerical results to Mustafa et al. [45] and found excellent agreement. It is detected that there is SFC shrinkage when boosting the  $fw, \lambda, Fr, M, Nr, \Gamma_T, Nt, \Gamma_C$  and  $E$ , and it upturns when enriching the  $Ri, R, Hg, Ec, Nb, \theta_n, \sigma^{**}, \delta$  and  $n$ . The heat transfer gradient (HTG) loses when strengthening the quantity of  $\lambda, Fr, M, Nr, Hg, Ec, Nt, \Gamma_C, \delta, n$  and  $E$ , and it upturns when enhancing the amount of  $fw, Ri, R, \Gamma_T, Nb, \theta_n$  and  $\sigma^{**}$ . The LSN proliferate when mounting the quantity of  $\lambda, Fr, M, Nr, R, Hg, Nb, \theta_n, \Gamma_c$  and  $\delta$ . The quite opposite trend is obtained when changing the presence of  $fw, Ri, Ec, \Gamma_T, Nt, \sigma^{**}, n$  and  $E$ .

**Table 1.** The skin friction coefficient, local Nusselt number and local Sherwood number for  $fw, \lambda, Fr, M, Ri$  and  $Nr$  for both fluids.

fw	$\lambda$	Fr	M	Ri	Nr	$\frac{1}{2} Cf \sqrt{Re}$		$Nu/\sqrt{Re}$		$Sh/\sqrt{Re}$	
						Casson	Williamson	Casson	Williamson	Casson	Williamson
−0.6	0.2	0.4	0.5	0.5	0.5	−0.509450	−0.391709	0.579321	0.583070	−0.325537	−0.327817
−0.3						−0.540008	−0.427964	0.641809	0.642974	−0.363858	−0.364580
0.0						−0.571635	−0.468255	0.708673	0.706679	−0.405644	−0.404386
0.3						−0.603205	−0.511666	0.779139	0.773945	−0.450585	−0.447240
0.6						−0.633606	−0.556634	0.852262	0.844421	−0.498239	−0.493078
0.4	0.0	0.4	0.5	0.5	0.5	−0.594642	−0.508055	0.806499	0.800459	−0.468292	−0.464370
	0.4					−0.629919	−0.543188	0.800562	0.794198	−0.464437	−0.460312
	0.8					−0.657162	−0.571883	0.796283	0.789413	−0.461663	−0.457217
	1.2					−0.679033	−0.595949	0.793056	0.785643	−0.459573	−0.454781
0.4	0.2	0.0	0.5	0.5	0.5	−0.603953	−0.514606	0.804272	0.798227	−0.466845	−0.462923

Table 1. Cont.

fw	$\lambda$	Fr	M	Ri	Nr	$\frac{1}{2}Cf\sqrt{Re}$		$Nu/\sqrt{Re}$		$Sh/\sqrt{Re}$		
						Casson	Williamson	Casson	Williamson	Casson	Williamson	
0.4	0.2	0.4	0.0	0.5	0.5	0.6	-0.617898	-0.532082	0.802808	0.796584	-0.465894	-0.461858
						1.2	-0.629722	-0.547022	0.801560	0.795165	-0.465084	-0.460939
						1.8	-0.639957	-0.560048	0.800480	0.737920	-0.464384	-0.460133
						0.5	-0.560068	-0.475720	0.812721	0.806599	-0.472339	-0.468357
						1.0	-0.613519	-0.526577	0.803268	0.797104	-0.466193	-0.462195
0.4	0.2	0.4	0.5	0.0	0.5	1.5	-0.650934	-0.565199	0.797237	0.790500	-0.462281	-0.457920
						0.4	-0.679033	-0.595949	0.793786	0.785643	-0.459573	-0.454781
						0.4	-0.660336	-0.580349	0.798424	0.788312	-0.463051	-0.456505
						0.7	-0.622571	-0.536848	0.802412	0.795557	-0.465637	-0.461193
						1.0	-0.595805	-0.506627	0.804836	0.799939	-0.467212	-0.464033
0.4	0.2	0.4	0.5	0.5	-1.0	0.5	-0.570084	-0.477980	0.806865	0.803636	-0.468530	-0.466432
						-0.5	-0.606275	-0.522759	0.808362	0.804310	-0.469503	-0.466870
						0.0	-0.608591	-0.523896	0.806752	0.802074	-0.468456	-0.465418
						0.5	-0.611002	-0.525165	0.805055	0.799680	-0.467353	-0.463865
						1.0	-0.613519	-0.526577	0.803268	0.797104	-0.466193	-0.462195
						1.0	-0.616151	-0.528155	0.801381	0.794318	-0.464969	-0.460390

Table 2. The skin friction coefficient, local Nusselt number and local Sherwood number for  $R, Hg, Ec, \Gamma_T, Nb, Nt$  and  $\theta_n$  for both fluids.

R	Hg	Ec	$\Gamma_T$	Nb	Nt	$\theta_n$	$\frac{1}{2}Cf\sqrt{Re}$		$Nu/\sqrt{Re}$		$Sh/\sqrt{Re}$		
							Casson	Williamson	Casson	Williamson	Casson	Williamson	
0.0	-0.5	0.4	0.1	0.5	0.5	1.2	-0.629685	-0.5443759	0.552386	0.545982	-0.552386	-0.545982	
0.4							-0.613519	-0.526577	0.803268	0.797104	-0.466193	-0.462195	
0.8							-0.600650	-0.513580	1.023377	1.017386	-0.411036	-0.408267	
1.2							-0.590235	-0.503470	1.221039	1.215175	-0.372078	-0.370007	
0.4	-0.4	0.4	0.1	0.5	0.5	1.2	-0.609973	-0.522867	0.776546	0.770393	-0.448914	-0.444955	
							-0.2	-0.600663	-0.513212	0.708901	0.702637	-0.405788	-0.401838
							0.0	-0.586188	-0.498333	0.608328	0.600989	-0.343240	-0.338747
							0.2	-0.560224	-0.471686	0.431109	0.417147	-0.237329	-0.229206
							0.4	-0.548398	-0.443644	0.248746	0.158094	-0.133635	-0.083938
0.4	-0.5	0.0	0.1	0.5	0.5	1.2	0.5	-0.616797	-0.530165	0.828958	0.830200	-0.482937	-0.483750
							1.0	-0.612698	-0.525686	0.796834	0.788861	-0.462020	-0.456860
							1.5	-0.608584	-0.521271	0.764598	0.747832	-0.441233	-0.430502
							0.4	-0.604457	-0.516918	0.732266	0.707121	-0.420586	-0.404665
							0.4	-0.612511	-0.525620	0.799275	0.793245	-0.463602	-0.459696
0.4	-0.5	0.4	0.0	0.5	0.5	1.2	0.2	-0.614542	-0.527555	0.807356	0.801051	-0.468849	-0.464754
							0.4	-0.616637	-0.529576	0.815834	0.809232	-0.474367	-0.470068
							0.6	-0.618798	-0.531690	0.824758	0.817834	-0.480190	-0.475670
							0.4	-0.624871	-0.534266	0.795002	0.784238	-2.304167	-2.269369
							0.5	-0.613519	-0.526577	0.803268	0.797104	-0.466193	-0.462195
						1.0	-0.612246	-0.525851	0.804174	0.798416	-0.233391	-0.231523	
						1.5	-0.611828	-0.525618	0.804470	0.798843	-0.155658	-0.154441	

Table 2. Cont.

R	Hg	Ec	$\Gamma_T$	Nb	Nt	$\theta_n$	$\frac{1}{2}Cf\sqrt{Re}$		$Nu/\sqrt{Re}$		$Sh/\sqrt{Re}$	
							Casson	Williamson	Casson	Williamson	Casson	Williamson
0.4	−0.5	0.4	0.1	0.5	0.5	1.2	−0.613519	−0.526577	0.803268	0.797104	−0.466193	−0.46295
					1.0	−0.614246	−0.526134	0.790345	0.783132	−0.915639	−0.906320	
					1.5	−0.614786	−0.525509	0.777196	0.768887	−1.347998	−1.331962	
					2.0	−0.615136	−0.524713	0.763870	0.754421	−1.763066	−1.738850	
0.4	−0.5	0.4	0.1	0.5	0.5	1.0	−0.617049	−0.530398	0.748078	0.741525	−0.487877	−0.483603
					1.2	−0.613519	−0.526577	0.803268	0.797104	−0.466193	−0.462195	
					1.4	−0.609177	−0.521923	0.871668	0.865948	−0.440864	−0.437192	
					1.6	−0.603889	−0.516328	0.956034	0.950777	−0.412023	−0.408740	

Table 3. The skin friction coefficient, local Nusselt number and local Sherwood number for  $\Gamma_c, \sigma^{**}, \delta, n$  and  $E$  for both fluids.

$\Gamma_C$	$\sigma^{**}$	$\delta$	n	E	$\frac{1}{2}Cf\sqrt{Re}$		$Nu/\sqrt{Re}$		$Sh/\sqrt{Re}$	
					Casson	Williamson	Casson	Williamson	Casson	Williamson
0.0	1.0	1.0	0.5	1.0	−0.613044	−0.526039	0.803508	0.797397	−0.466349	−0.462385
0.1					−0.613519	−0.526577	0.803268	0.797104	−0.466193	−0.462195
0.2					−0.613985	−0.527112	0.803024	0.796807	−0.466035	−0.462003
0.3					−0.614443	−0.528172	0.802775	0.796199	−0.465873	−0.461608
0.1	0.0	1.0	0.5	1.0	−0.621718	−0.537316	0.802043	0.793644	−0.465398	−0.459954
					−0.616422	−0.529896	0.803344	0.796616	−0.466243	−0.461879
					−0.614204	−0.527324	0.803393	0.797110	−0.466274	−0.462199
					−0.612990	−0.526016	0.803097	0.797019	−0.466082	−0.462140
0.1	1.0	0.0	0.5	1.0	−0.613684	−0.526784	0.803713	0.797484	−0.466482	−0.462441
					−0.613634	−0.526719	0.803572	0.797365	−0.466391	−0.462364
					−0.613585	−0.526657	0.803438	0.797250	−0.466303	−0.462290
					−0.613519	−0.526577	0.803268	0.797104	−0.466193	−0.462195
0.1	1.0	1.0	0.0	1.0	−0.613558	−0.526629	0.803468	0.797283	−0.466323	−0.462311
					−0.613519	−0.526577	0.803268	0.797104	−0.466193	−0.462195
					−0.613492	−0.526540	0.803029	0.796883	−0.466038	−0.462052
					−0.613478	−0.526520	0.802745	0.796615	−0.465854	−0.461878
0.1	1.0	1.0	0.5	0.0	−0.611041	−0.524071	0.802264	0.796452	−0.465541	−0.461773
					−0.613519	−0.526577	0.803268	0.797104	−0.466193	−0.462195
					−0.616499	−0.529962	0.803240	0.796521	−0.466175	−0.461817
					−0.618951	−0.533118	0.802802	0.795459	−0.465891	−0.461129

Table 4. Comparison of local Nusselt number when  $We = \lambda = Fr = R = \Gamma_T = Hg = \Gamma_C = 0$  and  $M = Nr = 0 : 5, Sc = 5$  and  $\delta = 1$  with Mustafa et al. [45].

Pr	Nt	E	$\sigma^{**}$	n	Ri	$Nu/\sqrt{Re}$	
						Ref. [45]	Present
2.0	0.5	1.0	1.0	0.5	0.5	0.706605	0.706604
4.0						0.935952	0.935955
7.0						1.132787	1.132788
10.0						1.257476	1.257482
5.0	0.1	1.0	1.0	0.5	0.5	1.426267	1.426269
						1.013939	1.013938
						0.846943	0.846928
						0.649940	0.649939
5.0	0.5	0.0	1.0	0.5	0.5	0.941201	0.941209
						1.013939	1.013943
						1.064551	1.064563
						1.114549	1.114191

Table 4. Cont.

<i>Pr</i>	<i>Nt</i>	<i>E</i>	$\sigma^{**}$	<i>n</i>	<i>Ri</i>	<i>Nu</i> / $\sqrt{Re}$	
						Ref. [45]	Present
5.0	0.5	1.0	0.0	0.5	0.5	1.145304	1.145301
			1.0			1.013939	1.013938
			2.0			0.926282	0.926281
			5.0			0.798671	0.798669
5.0	0.5	1.0	2.0	−1.0	0.5	1.030805	1.030804
			−0.5			0.999470	0.999468
			0.0			0.964286	0.964285
			1.0			0.886830	0.886830
10.0	0.5	1.0	2.0	0.5	0.0	1.032281	1.032280
					0.5	1.056704	1.056706
					3.0	1.154539	1.154538
					5.0	1.215937	1.215938

Figure 2a–d display the variances of fluid velocity versus *Ri*(a), *fw*(b),  $\lambda$ (c) and *M* (d). It is clearly shown that the fluid speed enhances when heightening the quantity of *Ri* and it depresses when mounting the quantity of *fw*,  $\lambda$  and *M* for both fluids. In addition, the velocity of the Casson nanofluid is low near the plate and high away from the plate compared to Williamson nanofluid. Physically, a larger quantity of *M* generates a drag force named the Lorentz force. This force leads to suppressing the fluid movement on a plate surface, and this causes a decline in the fluid speed and thinner momentum boundary layer. The fluid temperature variations on *R*(a), *Hg*(b),  $\Gamma_T$ (c) and *Ec*(d) for both fluids are illustrated in Figure 3a–d. It is acknowledged that the fluid warmness escalates when enhancing the *R* and *Hg* values, and it suppresses when the  $\Gamma_T$  and *Ec* values are rising. Physically, the presence of a radiation parameter has enriched the fluid thermal state, thereby strengthening the fluid warmness and thicker thermal boundary layer thickness. In addition, the greater availability of Eckert number creates a more robust viscous dissipation effect, which enriches the fluid warmness. Figure 4a–d show the consequences of  $\sigma^{**}$ (a), *fw*(b), *E*(c) and *Nt*(d) on nanoparticle concentration profile. It is seen that the nanoparticle concentration reduces when raising the values  $\sigma^{**}$ . A opposite behavior occurs for varying the values of *fw*, *E* and *Nt*. The skin friction coefficient for a distinct combination of *M*,  $\lambda$  and *fw* is presented in Figure 5a–d. It is found that the surface shear stress decays when enhancing the magnetic field and porosity parameter for both *fw* values. In addition, the Williamson nanofluid has a greater skin friction coefficient value than the Casson nanofluid. Figure 6a–d portrayed the changes of local Nusselt number for a distinct combination of values of *M*,  $\lambda$  and *fw*. It is concluded that the heat transfer gradient slowly depresses when increasing the magnetic field and porosity parameters for both *fw* values. The local Sherwood number for various combination of values of *M*,  $\lambda$  and *fw* is shown in Figure 7a–d. It is seen from these figures that the local Sherwood number slowly depresses when increasing the magnetic field and porosity parameters for both *fw* values.

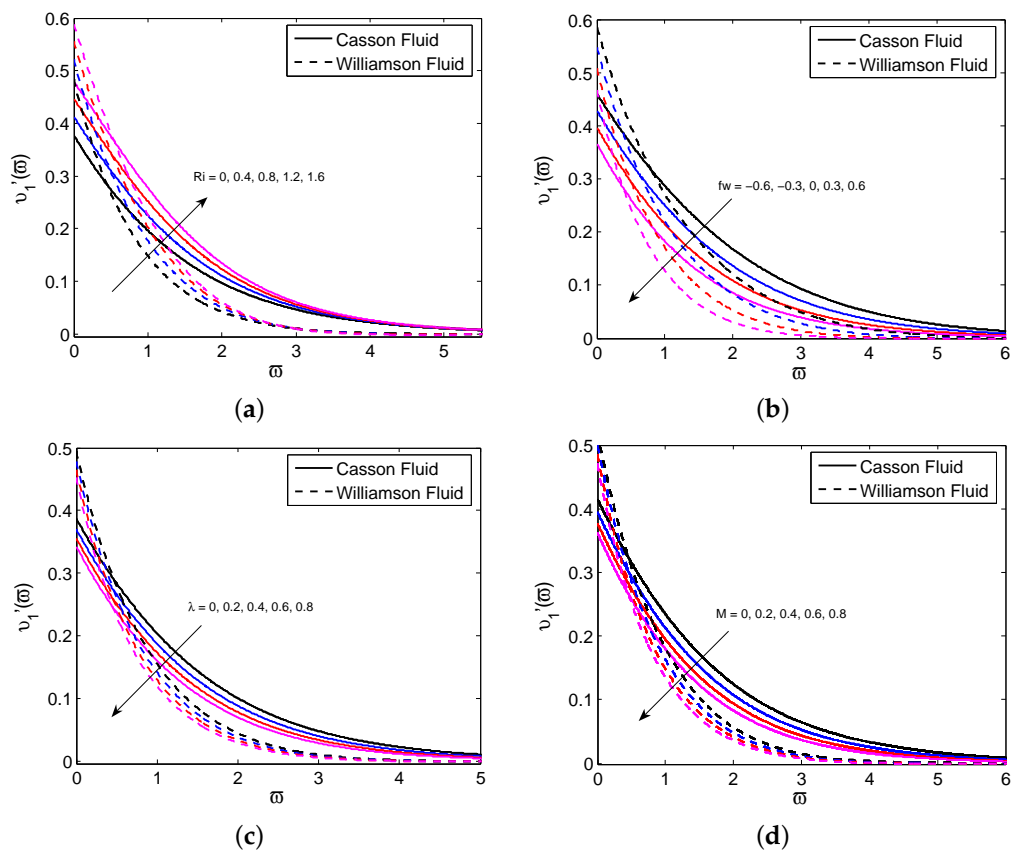


Figure 2. The nanofluid velocity for various values  $Ri$  (a),  $fw$  (b),  $\lambda$  (c) and  $M$  (d).

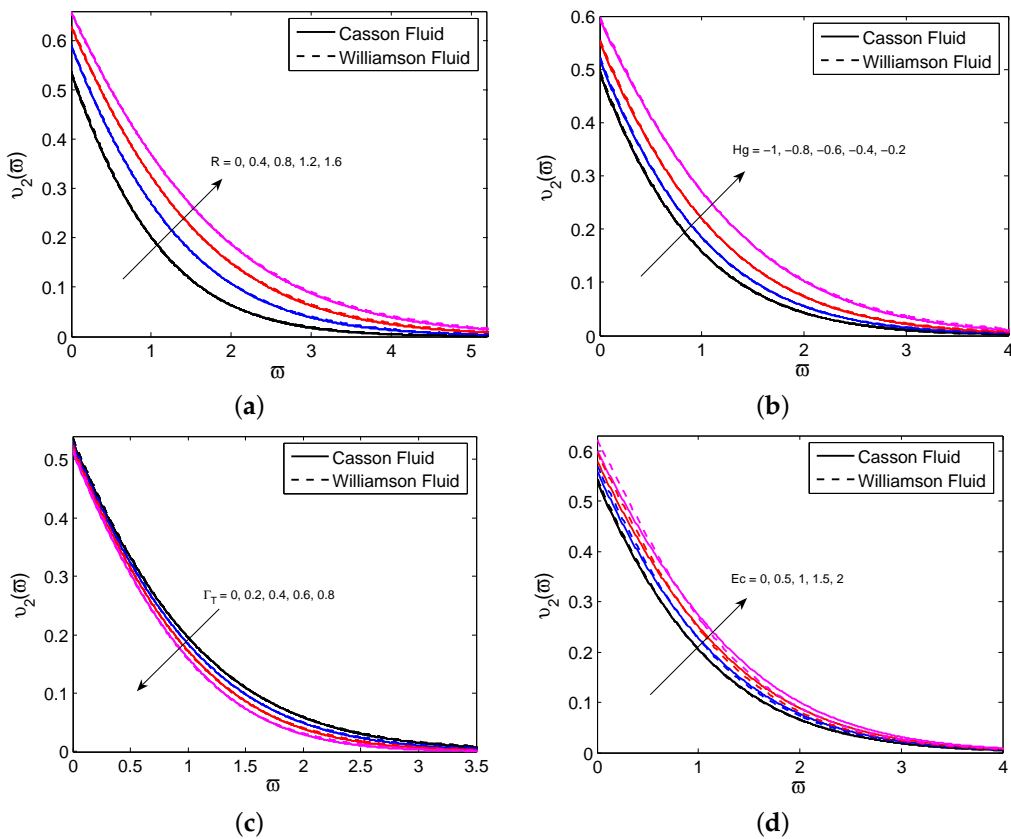


Figure 3. The nanofluid temperature profile for various vales of  $R$  (a),  $Hg$  (b),  $\Gamma_T$  (c) and  $Ec$  (d).

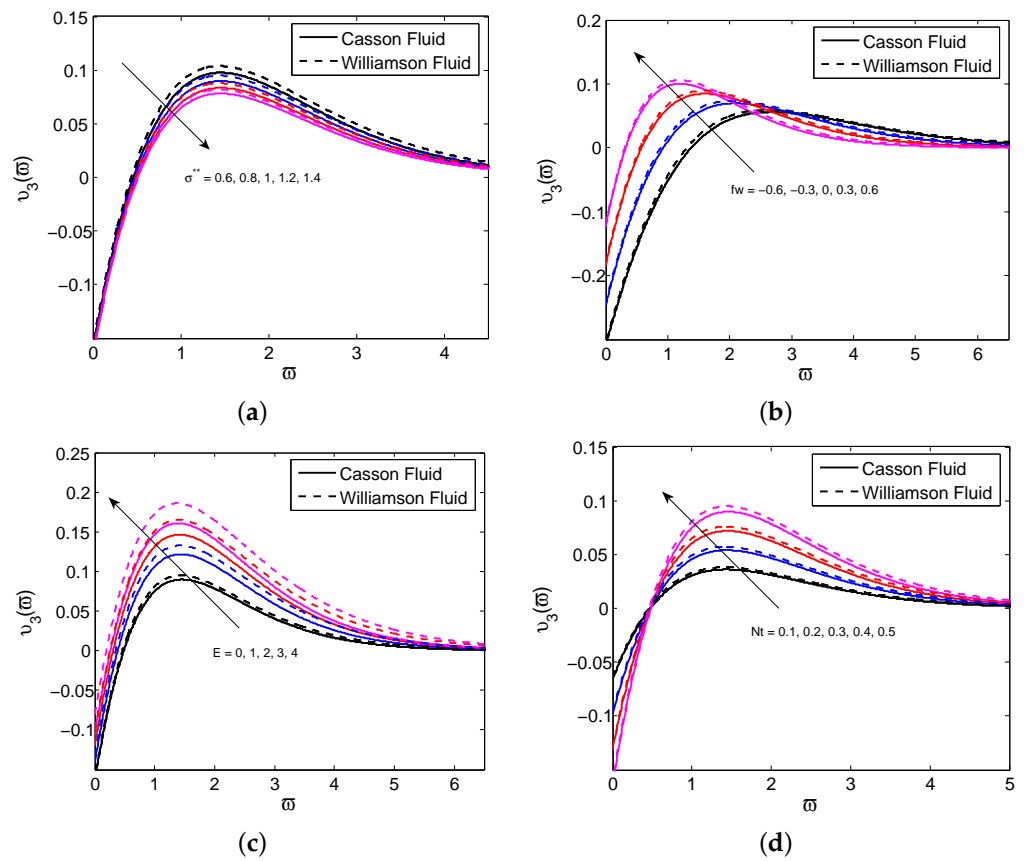


Figure 4. The nanoparticle concentration for various values of  $\sigma^{**}$  (a),  $fw$  (b),  $E$  (c) and  $Nt$  (d).

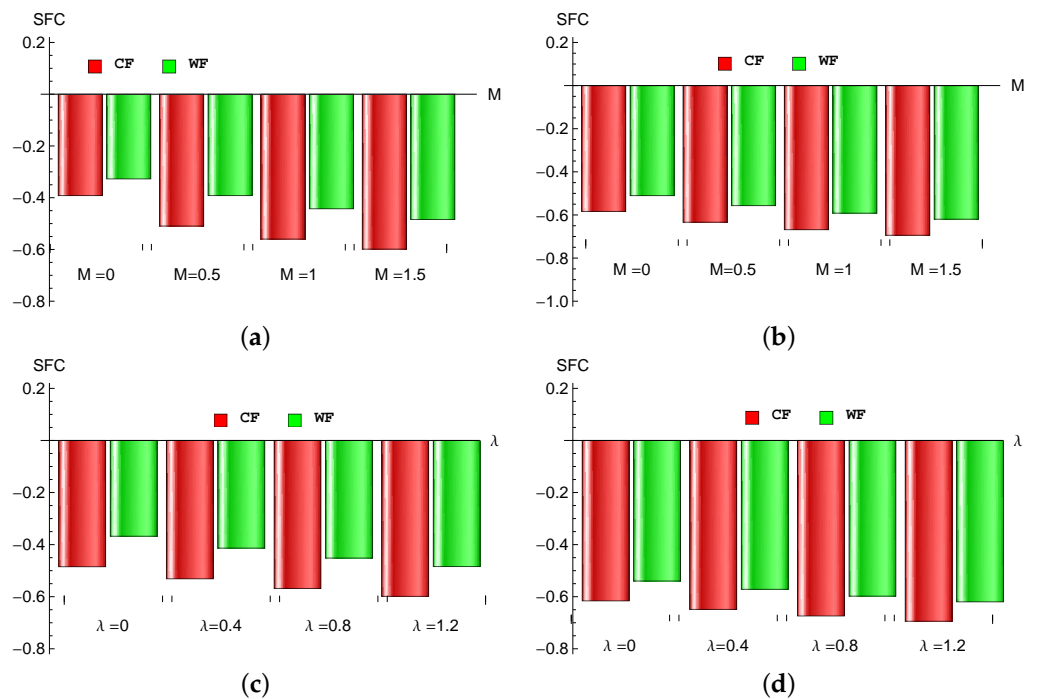
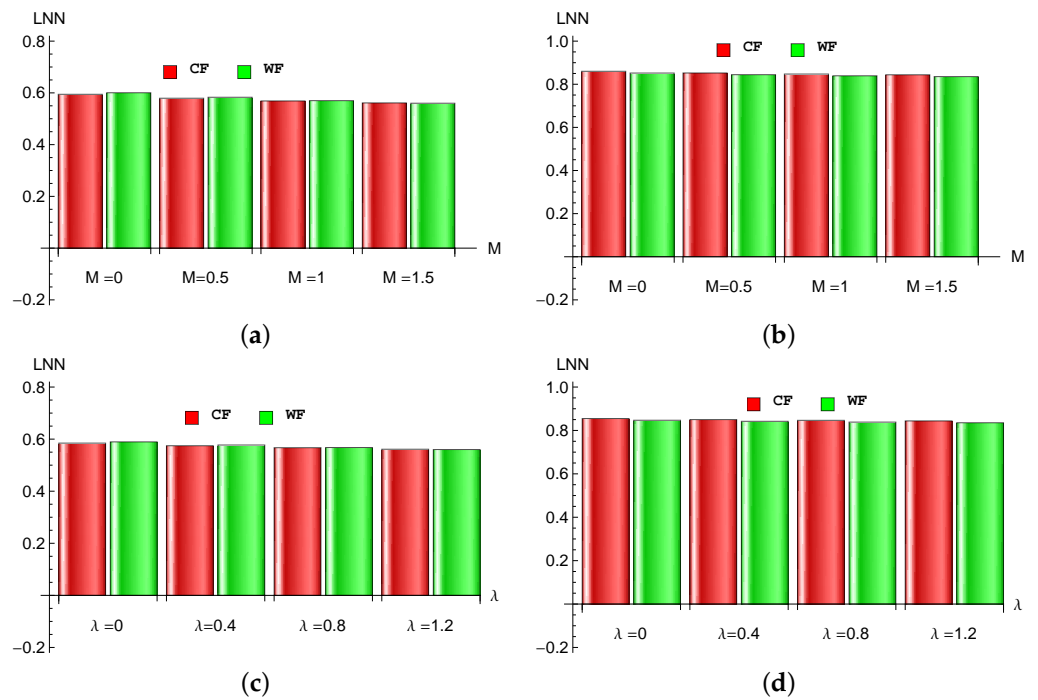
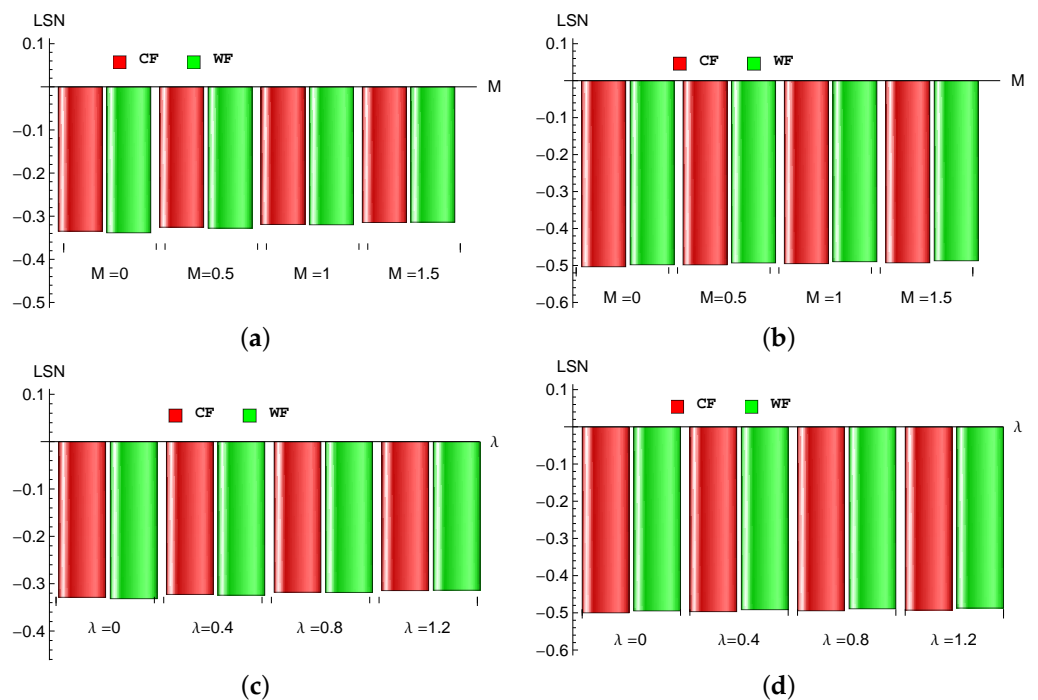


Figure 5. The skin friction coefficient (SFC) for different values of  $M$  with  $fw = -0.6$  (a),  $M$  with  $fw = 0.6$  (b),  $\lambda$  with  $fw = -0.6$  (c) and  $\lambda$  with  $fw = 0.6$  (d) for Casson nanofluid (CF) and Williamson nanofluid (WF).



**Figure 6.** The local Nusselt number (LNN) for different values of  $M$  with  $fw = -0.6$  (a),  $M$  with  $fw = 0.6$  (b),  $\lambda$  with  $fw = -0.6$  (c) and  $\lambda$  with  $fw = 0.6$  (d) for Casson nanofluid (CF) and Williamson nanofluid (WF).



**Figure 7.** The local Sherwood number (LSN) for different values of  $M$  with  $fw = -0.6$  (a),  $M$  with  $fw = 0.6$  (b),  $\lambda$  with  $fw = -0.6$  (c) and  $\lambda$  with  $fw = 0.6$  (d) for Casson nanofluid (CF) and Williamson nanofluid (WF).

**5. Conclusions**

Here, Brownian motion and the thermophoresis impact of the non-linear radiative flow of C-WNF in a Darcy–Forchheimer porous space with suction and heat consumption is investigated. The present investigation includes the consequences of activation energy

and binary chemical reaction. The governing mathematical models are numerically solved by the bvp4c algorithm with MATLAB. The main outcomes of our discussion are as follows:

- The fluid speed enhances for Richardson number but it slows against porosity, suction /injection and magnetic field parameters.
- The fluid becomes more warmed as the radiation, heat generation parameters and Eckert number increase.
- The nanoparticle concentration enhances upon strengthening the suction/injection and thermophoresis parameters and it downfalls upon escalating the reaction rate.
- The skin friction reduces after enriching the Forchheimer number, porosity and magnetic field parameters.
- The heat transfer gradient increases when escalating the values of radiation parameter and it downturns against radiation and heat generation parameters.
- The mass transfer gradient enhances upon heightening the Brownian motion parameter and it weakens against the thermophoresis parameter.
- In the future, we extend this flow model through the Riga plate with the convective heating condition.

**Author Contributions:** Data curation, S.E.; Formal analysis, K.L.; Investigation, S.T.; Methodology, S.E. and S.T. All authors have read and agreed to the published version of the manuscript.

**Funding:** This research received no external funding.

**Conflicts of Interest:** The authors declare no conflict of interest.

### Abbreviations

The following abbreviations are used in this manuscript:

#### Nomenclature

Symbols	Description
a,b	Positive constants
$B_0$	Magnetic field strength (T)
C	Fluid concentration ( $mol L^{-1}$ )
$C_b$	Drag coefficient
$C_p$	Specific heat ( $Jkg^{-1}K^{-1}$ )
$C_\infty$	Ambient fluid concentration
$D_B$	Brownian diffusion coefficient ( $m^2s^{-1}$ )
$D_T$	Thermophoretic diffusion coefficient
$E(= Ea/kT_\infty)$	Activation energy parameter
Ea	Activation energy
$Fr(= C_b/\sqrt{k_1})$	Forchheimer number
f	Dimensionless velocity
g	Acceleration due to gravity ( $ms^{-2}$ )
$Gr_x(= (g\beta(1 - C_\infty)(T_w - T_\infty)x^3/\nu^2)$	Local Grashof number
$Hg(= \frac{Q}{\rho_f C_p a})$	Heat generation/absorption parameter
k	Thermal conductive ( $Wm^{-1}K^{-1}$ )
$k_1$	Permeability of porous medium ( $m^2$ )
$k^*$	Mean absorption coefficient
kr	Reaction rate
$M(= \frac{\sigma B_0^2}{\rho_f a})$	Magnetic parameter
n	Fitted rate or stretching sheet index parameter
Ec	Eckert number
$Nb(= \frac{\tau D_B(C_w - C_\infty)}{\nu})$	Brownian diffusion parameter
$Nt(= \frac{\tau D_T(T_w - T_\infty)}{T_\infty \nu})$	Thermophoresis parameter
$Pr(= \frac{\nu}{\alpha} = \frac{m^2s^{-1}}{m^2s^{-1}} = 1)$	Prandtl number
Q	Heat generation/absorption coefficient ( $JM^{-1}m^{-3}s^{-1}$ )

$R(= \frac{4\sigma^* T_\infty^3}{kk^*})$	Thermal radiation
$Re_x(= \frac{U_\omega x}{\nu})$	Local Reynolds number
$Ri(= \frac{Gr_x}{Re_x^2} = \frac{g\beta(1-C_\infty)(T_\omega - T_\infty)}{a^2 x})$	Richardson number
$Sc(= \frac{\nu}{D_B})$	Schmith number
$T$	Fluid temperature (K)
$T_\infty$	Ambient temperature (K)
$u, v$	Velocity components ( $ms^{-1}$ )
$U_\omega$	Stretching surface velocity ( $ms^{-1}$ )
$We(= \Gamma x \sqrt{2a^3/\nu}) = sm \sqrt{\frac{2s^{-3}}{m^2 s^{-1}}} = \text{constant}$	Weissenberg number
$x, y$	Direction coordinates (m)
<b>Greek Symbols</b>	<b>Description</b>
$\alpha$	Thermal diffusivity ( $m^2 s^{-1}$ )
$\beta$	Casson parameter
$\delta(= \frac{T_\omega - T_\infty}{T_\infty})$	Temperature difference parameter
$\Gamma$	Williamson parameter or time constant
$\Gamma_T(= a\lambda_T)$	Thermal relaxation parameter
$\Gamma_C(= a\lambda_C)$	Solute relaxation parameter
$\lambda$	Local porosity parameter
$\lambda_C$	Relaxation time of mass flux
$\lambda_T$	Relaxation time of heat flux
$\nu$	Kinetic viscosity ( $m^2 s^{-1}$ )
$\phi$	Non-dimensional nanofluid concentration
$\rho_f$	Fluid density ( $kg m^{-3}$ )
$\sigma$	Electrical conductivity ( $S m^{-1}$ )
$\sigma^*$	Stefan–Boltzmann constant ( $W m^{-2} K^{-4}$ )
$\sigma^{**}(= \frac{kr^2}{a})$	Dimensionless reaction rate
$\tau$	Heat capacity ratio
$\theta$	Non-dimensional temperature
$\theta_n$	Temperature ratio parameter
$\eta$	Similarity variable
$\mu$	Dynamic viscosity ( $Kg m^{-1} s^{-1}$ )
$p$	Dust phase
$\infty$	Fluid properties at ambient condition

## References

- Elnaqeeb, T.; Animasaun, I.L.; Shah, N.A. Ternary-hybrid nanofluids: significance of suction and dual-stretching on three-dimensional flow of water conveying nanoparticles with various shapes and densities. *Z. Naturforsch. A* **2021**, *76*, 231–243. [\[CrossRef\]](#)
- Islam, T.; Yavuz, M.; Parveen, N.; Fayz-Al-Asad, M. Impact of non-uniform periodic magnetic field on unsteady natural convection flow of nanofluids in square enclosure. *Fractal Fract* **2022**, *6*, 101. [\[CrossRef\]](#)
- Saleem, S.; Animasaun, I.L.; Yook, S.J.; Al-Mdallal, Q.M.; Shah, N.A.; Faisal, M. Insight into the motion of water conveying three kinds of nanoparticles shapes on a horizontal surface: Significance of thermo-migration and Brownian motion. *Surf. Interfaces* **2022**, *30*, 101854. [\[CrossRef\]](#)
- Choi, S.U.S. Enhancing thermal conductivity of fluids with nanoparticles. *ASME-Publications-Fed* **1995**, *231*, 99–106.
- Sheikholeslami, M. Effect of uniform suction on nanofluid flow and heat transfer over a cylinder. *J. Braz. Soc. Mech. Sci. Eng.* **2015**, *37*, 1623–1633. [\[CrossRef\]](#)
- Ramana Reddy, J.V.; Sugunamma, V.; Sandeep, N. Thermophoresis and Brownian motion effects on unsteady MHD nanofluid flow over a slendering stretching surface with slip effects. *Alex. Eng. J.* **2018**, *57*, 2465–2473. [\[CrossRef\]](#)
- Makinde, O.D.; Mabood, F.; Khan, W.A.; Tshela, M.S.; MHD flow of a variable viscosity nanofluid over a radially stretching convective surface with radiative heat. *J. Mol. Liq.* **2016**, *219*, 624–630. [\[CrossRef\]](#)
- Shafey, A.M.E.; Alharbi, F.M.; Javed, A.; Abbas, N.; ALrafai, H.A.; Nadeem, S.; Issakhov, A. Theoretical analysis of Brownian and thermophoresis motion effects for Newtonian fluid flow over nonlinear stretching cylinder. *Case Stud. Therm. Eng.* **2021**, *28*, 101369. [\[CrossRef\]](#)
- Rasheed, H.U.; Islam, S.; Khan, Z.; Khan, J.; Mashwani, W.K.; Abbas, T.; Shah, Q. Computational analysis of hydromagnetic boundary layer stagnation point flow of nano liquid by a stretched heated surface with convective conditions and radiation effect. *Adv. Mech. Eng.* **2021**, *13*, 168781402111053142. [\[CrossRef\]](#)

10. Alotaibi, H.; Althubiti, S.; Eid, M.R.; Mahny, K.L. Numerical treatment of MHD flow of Casson nanofluid via convectively heated non-linear extending surface with viscous dissipation and suction/injection effects. *Comput. Mater. Continua* **2021**, *66*, 229–245. [[CrossRef](#)]
11. Nayak, M.K.; Prakash, J.; Tripathi, D.; Pandey, V.S.; Shaw S. 3D Bioconvective multiple slip flow of chemically reactive Casson nanofluid with gyrotactic microorganisms. *Heat Transf. Res.* **2020**, *49*, 135–153. [[CrossRef](#)]
12. Butt, A.S.; Maqbool, K.; Imran, S.M.; Ahmad, B. Entropy generation effects in MHD Casson nanofluid past a permeable stretching surface. *Int. J. Exergy* **2020**, *31*, 150–171. [[CrossRef](#)]
13. Ibrahim, S.M.; Lorenzini, G.; Vijaya Kumar, P.; Raju, C.S.K. Influence of chemical reaction and heat source on dissipative MHD mixed convection flow of a Casson nanofluid over a nonlinear permeable stretching sheet. *Int. J. Heat Mass Transf.* **2017**, *111*, 346–355. [[CrossRef](#)]
14. Afify, A.A. The influence of slip boundary condition on Casson nanofluid flow over a stretching sheet in the presence of viscous dissipation and chemical reaction. *Math. Probl. Eng.* **2017**, *2017*, 3804751. [[CrossRef](#)]
15. Varun Kumar, R.S.; Dhananjaya, P.G.; Naveen Kumar, R.; Punith Gowda, R.J.; Prasannakumara, B.C. Modeling and theoretical investigation on Casson nanofluid flow over a curved stretching surface with the influence of magnetic field and chemical reaction. *Int. J. Comput. Methods Eng. Sci. Mech.* **2022**, *23*, 12–19. [[CrossRef](#)]
16. Naveen Kumar, R.; Punith Gowda, R.J.; Madhukesh, J.K.; Prasannakumara, B.C.; Ramesh, G.K. Impact of thermophoretic particle deposition on heat and mass transfer across the dynamics of Casson fluid flow over a moving thin needle. *Phys. Scr.* **2021**, *96*, 075210. [[CrossRef](#)]
17. Khan, T.S.; Sene, N.; Mouldi, A.; Brahmia, A. Heat and mass transfer of the Darcy–Forchheimer Casson hybrid nanofluid flow due to an extending curved surface. *J. Nanomat.* **2022**, *2022*, 3979168.
18. Waqas, S.H.; Khan, S.U.; Imran, M.; Bhatti, M.M. Thermally developed Falkner–Skan bioconvection flow of a magnetized nanofluid in the presence of a motile gyrotactic microorganism: Buongiorno’s nanofluid model. *Phys. Scr.* **2019**, *94*, 115304. [[CrossRef](#)]
19. Li, Y.X.; Alshbool, M.H.; Lv, Y.P.; Khan, I.; Khan, M.R.; Issakhov, A. Heat and mass transfer in MHD Williamson nanofluid flow over an exponentially porous stretching surface. *Case Stud. Therm. Eng.* **2021**, *26*, 100975. [[CrossRef](#)]
20. Ahmed, K.; Akbar, T. Numerical investigation of magnetohydrodynamics Williamson nanofluid flow over an exponentially stretching surface. *Adv. Mech. Eng.* **2021**, *13*, 168781402110198. [[CrossRef](#)]
21. Iqbal, W.; Naeem, M.N.; Jalil, M. Numerical analysis of Williamson fluid flow along an exponentially stretching cylinder. *AIP Adv.* **2019**, *9*, 055118. [[CrossRef](#)]
22. Gorla, R.S.R.; Giresha, B.J. Dual solutions for stagnation-point flow and convective heat transfer of a Williamson nanofluid past a stretching/shrinking sheet. *Heat Mass Transf.* **2016**, *52*, 1153–1162. [[CrossRef](#)]
23. Srinivasulu, T.; Goud, B.S. Effect of inclined magnetic field on flow, heat and mass transfer of Williamson nanofluid over a stretching sheet. *Case Stud. Therm. Eng.* **2021**, *23*, 100819. [[CrossRef](#)]
24. Mahanta, G.; Das, M.; Nayak, M.K.; Shaw, S. Irreversibility Analysis of 3D Magnetohydrodynamic Casson Nanofluid Flow Past Through Two Bi-Directional Stretching Surfaces with Nonlinear Radiation. *J. Nanofluids* **2021**, *10*, 316–326. [[CrossRef](#)]
25. Humane, P.P.; Patil, V.S.; Patil, A.B. Chemical reaction and thermal radiation effects on magnetohydrodynamics flow of Casson–Williamson nanofluid over a porous stretching surface. *Proc. Inst. Mech. Eng. E: J. Process Mech. Eng.* **2021**, *235*, 2008–2018. [[CrossRef](#)]
26. Akinshilo, A.T.; Mabood, F.; Ilegbusi, A.O. Heat generation and nonlinear radiation effects on MHD Casson nanofluids over a thin needle embedded in porous medium. *Int. Commun. Heat Mass Transf.* **2021**, *127*, 105547. [[CrossRef](#)]
27. Ghasemi, S.E.; Mohsenian, S.; Gouran, S.; Zolfagharian, A. A novel spectral relaxation approach for nanofluid flow past a stretching surface in presence of magnetic field and nonlinear radiation. *Results Phys.* **2022**, *32*, 105141. [[CrossRef](#)]
28. Imran, M.; Farooq, U.; Muhammad, T.; Khan, S.U.; Waqas, H. Bioconvection transport of Carreau nanofluid with magnetic dipole and nonlinear thermal radiation. *Case Stud. Therm. Eng.* **2021**, *26*, 101129. [[CrossRef](#)]
29. Bhatti, M.M.; Abbas, T.; Rashidi, M.M. Numerical study of entropy generation with nonlinear thermal radiation on magnetohydrodynamics non-Newtonian nanofluid through a porous shrinking sheet. *J. Magn.* **2016**, *21*, 468–475. [[CrossRef](#)]
30. Mahanthesh, B.; Thriveni, K. Significance of inclined magnetic field on nano-bioconvection with nonlinear thermal radiation and exponential space based heat source: A sensitivity analysis. *Eur. Phys. J. Spec. Top.* **2021**, *230*, 1487–1501. [[CrossRef](#)]
31. Cao, W.; Animasaun, I.L.; Yook, S.J.; Oladipupo, V.A.; Ji, X. Simulation of the dynamics of colloidal mixture of water with various nanoparticles at different levels of partial slip: Ternary-hybrid nanofluid. *Int. Commun. Heat Mass Transf.* **2022**, *135*, 106069. [[CrossRef](#)]
32. Eswaramoorthi, S.; Divya, S.; Faisal, M.; Namgyel, N. Entropy and heat transfer analysis for MHD flow of-water-based nanofluid on a heated 3D plate with nonlinear radiation. *Math. Probl. Eng.* **2022**, *2022*, 7319988. [[CrossRef](#)]
33. Shah, Z.; Kumam, P.; Deebani, W. Radiative MHD Casson Nanofluid Flow with Activation energy and chemical reaction over past nonlinearly stretching surface through Entropy generation. *Sci. Rep.* **2020**, *10*, 4402. [[CrossRef](#)] [[PubMed](#)]
34. Aziz, S.; Ahmad, I.; Khan, S.U.; Ali, N. A three-dimensional bioconvection Williamson nanofluid flow over bidirectional accelerated surface with activation energy and heat generation. *Int. J. Mod. Phys. B* **2021**, *35*, 2150132. [[CrossRef](#)]
35. Kalaivanan, R.; Vishnu Ganesh, N.; Al-Mdallal, Q.M. An investigation on Arrhenius activation energy of second grade nanofluid flow with active and passive control of nanomaterials. *Case Stud. Therm. Eng.* **2020**, *22*, 100774. [[CrossRef](#)]

36. Zeeshan, A.; Mehmood, O.U.; Mabood, F.; Alzahrani, F. Numerical analysis of hydromagnetic transport of Casson nanofluid over permeable linearly stretched cylinder with Arrhenius activation energy. *Int. Commun. Heat Mass Transf.* **2022**, *130*, 105736. [[CrossRef](#)]
37. Tayyab, M.; Siddique, I.; Jarad, F.; Ashraf, M.K.; Ali, B. Numerical solution of 3D rotating nanofluid flow subject to Darcy–Forchheimer law, bio-convection and activation energy. *S. Afr. J. Chem. Eng.* **2022**, *40*, 48–56. [[CrossRef](#)]
38. Rashid, S.; Hayat, T.; Qayyum, S.; Ayub, M.; Alsaedi, A. Three dimensional rotating Darcy–Forchheimer flow with activation energy. *Int. J. Numer. Methods Heat Fluid Flow* **2018**, *29*, 935–948. [[CrossRef](#)]
39. Alsaadi, F.E.; Hayat, T.; Khan, M.I.; Alsaadi, F.E. Heat transport and entropy optimization in flow of magneto-Williamson nanomaterial with Arrhenius activation energy. *Comput. Methods Progr. Biomed.* **2020**, *183*, 105051. [[CrossRef](#)]
40. Punith Gowda, R.J.; Naveen Kumar, R.; Jyothi, A.M.; Prasannakumara, B.C.; Sarris, I.E. Impact of binary chemical reaction and activation energy on heat and mass transfer of marangoni driven boundary layer flow of a non-Newtonian nanofluid. *Processes* **2021**, *9*, 702. [[CrossRef](#)]
41. Varun Kumar, R.S.; Alhadhrami, A.; Punith Gowda, R.J.; Naveen Kumar, R.; Prasannakumara, B.C. Exploration of Arrhenius activation energy on hybrid nanofluid flow over a curved stretchable surface. *ZAMM-J. Appl. Math. Mech./Z. Angew. Math. Mech.* **2021**, *101*, e202100035. [[CrossRef](#)]
42. Tamilzharasan, B.M.; Karthikeyan, S.; Kaabar, M.K.; Yavuz, M.; Özköse, F. Magneto Mixed Convection of Williamson Nanofluid Flow through a Double Stratified Porous Medium in Attendance of Activation Energy. *Math. Comput. Appl.* **2022**, *27*, 46. [[CrossRef](#)]
43. Nadeem, S.; Hussain, S.T. Flow and heat transfer analysis of Williamson nanofluid. *Appl. Nanosci.* **2014**, *4*, 1005–1012. [[CrossRef](#)]
44. Raju, C.S.K.; Sandeep, N.; Ali, M.E.; Nuhait, A.O. Heat and mass transfer in 3-D MHD Williamson–Casson fluids flow over a stretching surface with non-uniform heat source/sink. *Therm. Sci.* **2019**, *23*, 281–293. [[CrossRef](#)]
45. Mustafa, M.; Khan, J.A.; Hayat, T.; Alsaedi, A. Buoyancy effects on the MHD nanofluid flow past a vertical surface with chemical reaction and activation energy. *Int. J. Heat Mass Transf.* **2017**, *108*, 1340–1346. [[CrossRef](#)]
46. Ali, F.; Loganathan, K.; Eswaramoorthi, S.; Prabu, K.; Zaib, A.; Chaudhary, D.K. Heat transfer analysis on Carboxymethyl cellulose water-based cross hybrid nanofluid flow with entropy generation. *J. Nanomater.* **2022**, *2022*, 5252918. [[CrossRef](#)]
47. Eswaramoorthi, S.; Loganathan, K.; Jain, R.; Gyeltshen, S. Darcy–Forchheimer 3D flow of glycerin-based carbon nanotubes on a Riga plate with nonlinear thermal radiation and Cattaneo–Christov heat flux. *J. Nanomater.* **2022**, *2022*, 5286921. [[CrossRef](#)]